COMMUNICATION

Structure of KCNH2 cyclic nucleotide-binding homology domain reveals a functionally vital salt-bridge

Ariel Ben-Bassat[1], Moshe Giladi[1] [iD], and Yoni Haitin[1,2] [iD]

Human KCNH2 channels (hKCNH2, ether-à-go-go [EAG]–related gene, hERG) are best known for their contribution to cardiac action potential repolarization and have key roles in various pathologies. Like other KCNH family members, hKCNH2 channels contain a unique intracellular complex, consisting of an N-terminal eag domain and a C-terminal cyclic nucleotide-binding homology domain (CNBHD), which is crucial for channel function. Previous studies demonstrated that the CNBHD is occupied by an intrinsic ligand motif, in a self-liganded conformation, providing a structural mechanism for the lack of KCNH channel regulation by cyclic nucleotides. While there have been significant advancements in the structural and functional characterization of the CNBHD of KCNH channels, a high-resolution structure of the hKCNH2 intracellular complex has been missing. Here, we report the 1.5 Å resolution structure of the hKCNH2 channel CNBHD. The structure reveals the canonical fold shared by other KCNH family members, where the spatial organization of the intrinsic ligand is preserved within the β-roll region. Moreover, measurements of small-angle x-ray scattering profile in solution, as well as comparison with a recent NMR analysis of hKCNH2, revealed high agreement with the crystallographic structure, indicating an overall low flexibility in solution. Importantly, we identified a novel salt-bridge (E807-R863) which was not previously resolved in the NMR and cryo-EM structures. Electrophysiological analysis of charge-reversal mutations revealed the bridge's crucial role in hKCNH2 function. Moreover, comparison with other KCNH members revealed the structural conservation of this salt-bridge, consistent with its functional significance. Together with the available structure of the mouse KCNH1 intracellular complex and previous electrophysiological and spectroscopic studies of KCNH family members, we propose that this salt-bridge serves as a strategically positioned linchpin to support both the spatial organization of the intrinsic ligand and the maintenance of the intracellular complex interface.

Introduction

Human KCNH2 (hKCNH2; the human ether-à-go-go [EAG]–related gene), also known as hERG1, is a member of the KCNH voltage-dependent delayed rectifier potassium channel family. Best known for their critical role in cardiac action potential repolarization (Sanguinetti and Jurkiewicz, 1990; Curran et al., 1995; Sanguinetti et al., 1995; Trudeau et al., 1995), these channels are important regulators of cellular excitability (Warmke et al., 1991; Ganetzky et al., 1999). Moreover, hKCNH2s have key roles in cardiac pathologies (Sanguinetti and Tristani-Firouzi, 2006), as well as neuronal and mental diseases such as schizophrenia (Huffaker et al., 2009). Importantly, these channels are notoriously sensitive to adverse drug interactions, resulting in drug-induced long QT syndrome (LQTS; Sanguinetti and

Tristani-Firouzi, 2006), a potentially lethal cardiac disorder, and are known to harbor numerous LQTS-related mutations (Curran et al., 1995). Finally, similar to other KCNH family members, hKCNH2 expression was demonstrated in various tumors (Bianchi et al., 1998), possibly indicating additional noncanonical pathophysiological roles.

Composed of four identical subunits surrounding a centrally located ion conductive pore, each hKCNH2 subunit demonstrates the characteristic voltage-dependent potassium channel topology, consisting of six membrane-spanning domains with cytoplasmic N- and C-termini (Warmke et al., 1991). However, unique to the KCNH channels family, the N-terminal region contains an eag domain and the C-terminal region contains a

---

[1]Department of Physiology and Pharmacology, Sackler Faculty of Medicine, Tel Aviv University, Tel Aviv, Israel; [2]Sagol School of Neuroscience, Tel Aviv University, Tel Aviv, Israel.

Correspondence to Yoni Haitin: yhaitin@tauex.tau.ac.il.

Check for updates

cyclic nucleotide-binding homology domain (CNBHD), with both domains forming an intracellular complex crucial for channel function (Morais Cabral et al., 1998; Gustina and Trudeau, 2009; Haitin et al., 2013). Importantly, it has recently become clear that many of the specialized gating properties of KCNH channels arise from their structurally distinct intracellular domains (Morais-Cabral and Robertson, 2015). Indeed, many LQTS-related mutations are scattered throughout the intracellular complex, suggesting it plays critical roles during protein biogenesis, trafficking, and function (Chen et al., 1999; Anderson et al., 2006; Harley et al., 2012).

While the CNBHD of KCNH channels shows a high level of structural conservation with the cyclic nucleotide-binding domain (CNBD) of hyperpolarization-activated cyclic nucleotide–gated (HCN) channels, it does not bind cyclic nucleotides (Robertson et al., 1996; Brelidze et al., 2009). Instead, recent molecular structures of multiple KCNH homologues revealed that the cyclic nucleotide-binding pocket within the CNBHD is occupied by a short β-strand fold, termed the intrinsic ligand, perfectly mimicking the occupancy of cyclic nucleotides within the CNBD of HCN channels (Brelidze et al., 2012; Marques-Carvalho et al., 2012; Haitin et al., 2013). Critically, the discovery that the CNBHD of KCNH channels is in a self-liganded conformation was not predicted by mere sequence analyses and resulted directly from structural studies of this domain. Moreover, this short three-residue stretch was recently shown to be involved in shaping the gating properties of KCNH1 channels (Zhao et al., 2017), suggesting a mechanistic role for the otherwise functionally orphan CNBHD.

The recent "resolution revolution" of single-particle cryo-EM did not skip the KCNH channels family (Whicher and MacKinnon, 2016; Wang and MacKinnon, 2017). However, while providing groundbreaking insights into the architecture of the intact channel, the resolution ranged between ~4.5 and 5.5 Å at the cytosolic eag domain and CNBHD. Thus, the derivation of atomic resolution details regarding the organization of the intrinsic ligand is limited. Here, we used size-exclusion chromatography combined with multi-angle light scattering (SEC-MALS), x-ray crystallography, and small-angle x-ray scattering (SAXS) to characterize the structural properties of the CNBHD of hKCNH2. Our results provide the first high-resolution crystal structure of hKCNH2, resolved at 1.5 Å resolution. In agreement with the available structural information, the structure reveals that the CNBHD of hKCNH2 shares a similar fold with other members of the family. Accordingly, the spatial organization of the intrinsic ligand is preserved within the canonical β-roll region (Brelidze et al., 2012, 2013; Marques-Carvalho et al., 2012). Intriguingly, comparison of our x-ray structure with a previously determined NMR ensemble (Li et al., 2016) suggests the presence of highly labile regions within this domain. However, followed by ensemble optimization method (EOM) analysis, SAXS data showed good agreement between the solution properties and the crystal structure, indicating the CNBHD of hKCNH2 is overall highly rigid. Finally, the crystal structure revealed the presence of a previously overlooked, strategically located salt-bridge, stabilizing the intrinsic ligand. Importantly, electrophysiological analyses of charge-reversal mutants revealed its crucial role for normal channel function.

Materials and methods
Protein expression and purification
The CNBHD (residues 734–864) of *hKCNH2* (GenBank accession no. NM_000238.3) was sub-cloned using 5′ NcoI and 3′ HindIII sites into a pETM11 vector containing an N-terminal hexa-histidine affinity tag followed by a tobacco etch virus protease (TEV) cleavage site and a Gly-Ala-Met-Gly cloning sequence. The construct was verified by sequencing. The protein was overexpressed and purified as previously described (Haitin et al., 2013), using immobilized metal affinity chromatography and SEC. Briefly, *Escherichia coli* T7 express competent cells (New England Biolabs), transformed with the CNBHD construct, were grown in Terrific Broth medium at 37°C until reaching OD_{600nm} = 0.6 and induced at 16°C by adding 0.25 mM isopropyl β-D-1-thiogalactopyranoside (Formedium). Proteins were expressed at 16°C for 16–20 h and harvested by centrifugation (10,000×g for 10 min). Cells were resuspended in buffer A containing (in mM) 150 NaCl, 50 Bis-Tris, pH 6.5, and 1 tris (2-carboxyethyl)phosphine supplemented with 15 mM imidazole, 2.5 µg ml⁻¹ DNaseI, 5 mM $MgCl_2$, 10 mg lysozyme, 1 mM PMSF, and Protease Inhibitor Cocktail Set III (Calbiochem). Cells were lysed with an EmulsiFlex-C3 homogenizer (Avestin), and the lysate was cleared by centrifugation at 32,000×g for 45 min at 4°C. The supernatant was then loaded onto a Ni^{2+} affinity resin column (HisTrap HP; GE Healthcare) followed by washing with buffer A containing 27 mM imidazole and eluted using buffer A supplemented with 300 mM imidazole. The hexa-histidine tag was removed by TEV cleavage overnight at 4°C. Imidazole was removed using a HiPrep 26/10 desalting column (GE Healthcare) equilibrated with buffer A containing 15 mM imidazole. The cleaved protein was loaded onto a second Ni^{2+} column with 15 mM imidazole to remove the cleaved hexa-histidine tag and TEV protease. The flow-through was collected, concentrated to 4–5 ml, and loaded onto a HiLoad 16/60 Superdex 75 column (GE Healthcare) equilibrated with gel filtration buffer containing (in mM) 150 NaCl, 5 dithiothreitol, and 20 Bis-Tris, pH 6.5. Finally, pooled fractions were concentrated to ~220 µM (3.3 mg/ml) using a 3-kD molecular weight cutoff concentrator (EMD-Millipore), flash-frozen in liquid N_2, and stored at –80°C until use.

SEC-MALS analysis
Experiments were performed on an HPLC system (Shimadzu) equipped with autosampler and UV detector, using a preequilibrated analytical SEC column (Superdex 200 10/300 GL; GE Healthcare) with gel filtration buffer. A sample of the purified CNBHD (2 mg/ml, 50 µl) was loaded onto the column and analyzed using an inline eight-angle light-scattering detector, followed by a differential refractive-index detector (Wyatt Technology). Refractive index and MALS readings were analyzed using the Astra software package (Wyatt Technology) to determine the molecular mass.

Protein crystallization and data collection
Crystals of the CNBHD were grown at 19°C using sitting-drop vapor diffusion by mixing a 1:1 ratio (vol/vol; Mosquito; TTP Labtech) of protein solution at 200 µM and a reservoir solution containing 20% (wt/vol) PEG 3350, 2% (vol/vol) Tacsimate, and 0.1 M Bis-Tris, pH 6.8. This condition produced crystals within

2 d, which grew to a maximum size of ∼200 × 100 × 100 µm after 7 d. For diffraction data collection, crystals were immersed in liquid N_2 after cryoprotection with 20% glycerol. Data were collected at 100°K on beamline ID23-1 of the European Synchrotron Radiation Facility (ESRF) using a wavelength of 0.972 Å. Integration, scaling, and merging of the diffraction data were performed using the XDS program (Collaborative Computational Project Number 4, 1994). The crystals belonged to space group $C222_1$ (a = 57.49 Å, b = 90.65 Å, and c = 61.11 Å, with α = β = γ = 90°).

Structure determination
The structure was solved by molecular replacement using the programs PHASER (McCoy, 2007) and PHENIX (Adams et al., 2010), using a modified chain A of the KCNH1 intracellular complex structure (Protein Data Bank accession no. 4LLO) as the search model. Data collection and refinement statistics are summarized in Table 1. Each asymmetric unit contained a single protein chain. Iterative model building and refinement were performed in PHENIX with manual adjustments using COOT (Emsley and Cowtan, 2004). All structural illustrations were prepared with University of California, San Francisco Chimera (Pettersen et al., 2004; https://www.cgl.ucsf.edu/chimera).

SAXS data collection and analysis
SAXS data were measured at beamline BM29 of the ESRF. Data were collected at 5°C with the x-ray beam at wavelength λ = 1.0 Å, and the distance from the sample to the detector (PILATUS 1 M; Dectris Ltd) was 2.867 m, covering a scattering vector range (q = 4 πsinθ/λ) from 0.0025 to 0.5 Å^{-1}. 10 frames of 2D images were recorded for each buffer or sample, with an exposure time of 1 s/frame. The 2D images were reduced to one-dimensional scattering profiles, and the scattering of the buffer was subtracted from the sample profile using the software on-site. Samples were analyzed in gel filtration buffer. To account for possible interparticle effects, each sample was measured at three concentrations (Table 2). The lowest concentration curve was merged with a higher concentration curve at q ∼0.2 Å^{-1} to prevent distortion of the low-angle data while preserving high signal-to-noise ratio at the higher angles, which are far less sensitive to interparticle effects (Koch et al., 2003). The experimental radius of gyration (R_g) was calculated from data at low q values in the range of $qRg < 1.3$, according to the Guinier approximation $\ln I(q) \approx \ln(I_0) - R_g 2q2/3$, using PRIMUS (Konarev et al., 2003). The Porod volume was derived from the paired-distance distribution function $P(r)$ calculated using GNOM (Petoukhov et al., 2012). The solution scattering of the crystal structure was calculated using CRYSOL (Svergun et al., 1995).

EOM analysis
The software RANCH (Bernadó et al., 2007) was used to generate a pool of 10,000 stereochemically feasible structures with a random linker between the α'F and αA. This pool was used as input for GAJOE (Bernadó et al., 2007), which selects an ensemble with the best fit to the experimental data using a genetic algorithm: 50 ensembles of 20 orientations each were "crossed" and "mutated" for 1,000 generations, and the process was repeated 50 times.

Table 1.   **Crystallographic statistics**

Data collection	
Space group	$C222_1$
Cell dimensions	
a, b, c (Å)	57.49, 90.65, 61.11
α, β, γ (°)	90, 90, 90
Beamline	ESRF ID23-1
Wavelength (Å)	0.972
Resolution (Å)	1.5
Multiplicity	11.48
Completeness (%)	99.7
Mean $I/\sigma(I)$	13.91
R_{merge} (%)	11.4
Refinement statistics	
No. of reflections (work/free)	24,578/1,297
Resolution range	45.3–1.5
R_{work}/R_{free}	0.1756/0.1874
No. of atoms	
Macromolecules	1,068
Solvent	283
Average B-factors	
Macromolecules	16.37
Solvent	32.77
RMS deviations	
Bond lengths (Å)	0.007
Bond angles (°)	1.26
Ramachandran outliers (%)	0

RMS, root mean square.

Two-electrode voltage clamp
Oocytes were obtained by surgical removal of ovary pieces from *Xenopus laevis* frogs (Xenopus 1) anesthetized with 0.15% tricaine (Sigma-Aldrich). The procedures for surgery and maintenance of frogs were approved by the animal research ethics committee of Tel Aviv University and in accordance with the Guide for the Care and Use of Laboratory Animals (National Academy of Sciences, Washington, DC). Oocytes were de-folliculated using 1 mg/ml collagenase (type IA; Sigma-Aldrich) in Ca^{2+}-free ND96 solution containing (in mM) 96 NaCl, 2 KCl, 1 $MgCl_2$, and 5 HEPES, pH 7.5 (ND96), for ∼1 h. Stage V and VI oocytes were selected for DNA injection and maintained at 18°C in ND96, supplemented with 1 mM pyruvate and 50 µg/ml gentamycin. For channel expression, intranuclear injections of 100 ng/µl hKCNH2 cDNA (in pcDNA3 vector; 10 nl per oocyte) were performed using a Nanoject injector (Drummond). Standard two-electrode voltage-clamp measurements were performed at room temperature (22–24°C) 2–5 d after DNA microinjections. Oocytes were placed into a 100-µl recording chamber and perfused with a modified ND96 solution (containing 0.1 mM $CaCl_2$). Whole-cell

Table 2. Data collection and scattering-derived parameters

Data collection parameters	
Sample	hKCNH2 734–864
Beamline	ESRF BM29
Beam geometry (mm²)	0.7 × 0.7
Wavelength (Å)	1.0
Q range (Å⁻¹)	0.0025–0.5
No. of frames	10
Exposure per frame (s)	0.5
Concentration (mg/ml)	3.0, 1.5, 0.7
Temperature (°C)	5
Structural parameters	
I_0 (from Guinier)[a]	11.3 ± 0.1
R_g (Å; from Guinier)[a]	15.9 ± 0.2
Porod volume (10^3 Å³)	27.23
χ^2 CRYSOL	1.4
χ^2 EOM	0.8
Software employed	
Primary data reduction	AUTOMAR
Data processing	PRIMUS
Modeling	CRYSOL, EOM

[a] ± SE

currents were recorded using a GeneClamp 500 amplifier through the pCLAMP 9.2.1.9 software (Axon Instruments, Inc.). Glass microelectrodes (A-M Systems, Inc.) were filled with 3 M KCl and had tip resistances of 0.2–1 MΩ. Current signals were digitized at 1 kHz and low-pass filtered at 0.2 kHz. The holding potential was –80 mV. Leak subtraction was performed off-line while assuming that the channels are closed at –80 mV and below. Errors introduced by the series resistance of the oocytes were not corrected and were minimized by keeping expression of the currents below 10 µA. The steady-state voltage dependence of activation (G–V) was measured by plotting the tail current amplitude versus the previous test pulse voltage and fit with a Boltzmann function:

$$ y = \frac{1}{\left[1 + e^{\left(\frac{V_{50} - V}{s} \right)} \right]}, $$

where V_{50} is the half-maximal activation potential and s is the slope factor. All data are presented as mean ± SEM, and n represents the number of cells. Current deactivation was fit with a double-exponential function:

$$ y = A_{fast} e^{-t/\tau_{fast}} + A_{slow} e^{-t/\tau_{slow}}, $$

where t is time and τ is the time constant of deactivation.

Statistical analyses were performed using repeated-measures two-way ANOVA. $P < 0.05$ was considered statistically significant.

Atomic coordinates and structure factors have been deposited in the Protein Data Bank with accession no. 6SYG.

Online supplemental material

Fig. S1 shows the results of employing an EOM analysis using the NMR ensemble to fit the experimentally determined hKCNH2 CNBHD scattering data. Fig. S2 shows the superposition of the hKCNH2 cryo-EM map and all the available structures of the CNBHD.

Results

Structural characterization of the CNBHD of hKCNH2

To elucidate the molecular organization of the CNBHD of hKCNH2, we first designed a soluble construct, amiable for downstream purification and crystallization. Specifically, similar to the strategy previously used for structural studies of the CNBHD of *Mus musculus* (mouse) KCNH1 (mKCNH1; mEAG1; Marques-Carvalho et al., 2012; Haitin et al., 2013), we truncated most of the C-linker, connecting the S6 and the CNBHD (Marques-Carvalho et al., 2012), and terminated the construct just downstream of the intrinsic ligand (Brelidze et al., 2012). This construct, termed CNBHD hereafter, spans residues 734–864 and consists of a remaining C-linker segment (734–747) and the full-length CNBHD (748–864; Fig. 1 A).

Next, using SEC-MALS, we determined that the purified CNBHD is monodispersed with a molecular mass of 14.3 ± 0.6 kD (Fig. 1 B), close to the calculated mass of the protein (14,929.22 D). Thus, in the absence of a C-linker, the CNBHD of hKCNH2 is monomeric in solution, similar to the observed stoichiometry of purified CNBHDs from other members of the KCNH family (Brelidze et al., 2012, 2013; Marques-Carvalho et al., 2012).

Following purification and solution characterization, we proceeded with CNBHD crystallization. The CNBHD of hKCNH2 readily crystallized in the space group C222₁ with a single molecule in the asymmetric unit and diffracted x rays to 1.5 Å resolution (Table 1). The structure was solved by molecular replacement, using the CNBHD of mKCNH1 intracellular complex (Haitin et al., 2013) as a search model. The structure of the CNBHD of hKCNH2 (Fig. 1 C) can be subdivided into four distinct segments: (1) the remnant C-linker, composed of helices α′E and α′F, organized in a helix-turn-helix configuration; (2) the β-roll, situated between the αA and αB helices featuring the canonical eight β-strand fold (β1–β8), which mediates ligand binding in HCN and cyclic nucleotide-gated ion channels (Craven and Zagotta, 2006); (3) the C-helix (helix αC), which, together with αB, flanks the β-roll and was shown to underlie ligand-induced gating enhancement of cyclic nucleotide-gated channels (Puljung and Zagotta, 2013); and (4) the KCNH family unique intrinsic ligand, consisting of a short β-strand (β9; Fig. 1 D), which is involved in the formation of the interaction interface with the N-terminal eag domain (Haitin et al., 2013; Wang and MacKinnon, 2017) and differentially affects KCNH channel activation (Zhao et al., 2017) and deactivation (Codding and Trudeau, 2019). Together, the overall fold of the CNBHD of hKCNH2 is reminiscent of that observed in other CNBD-containing proteins (Rehmann et al., 2007).
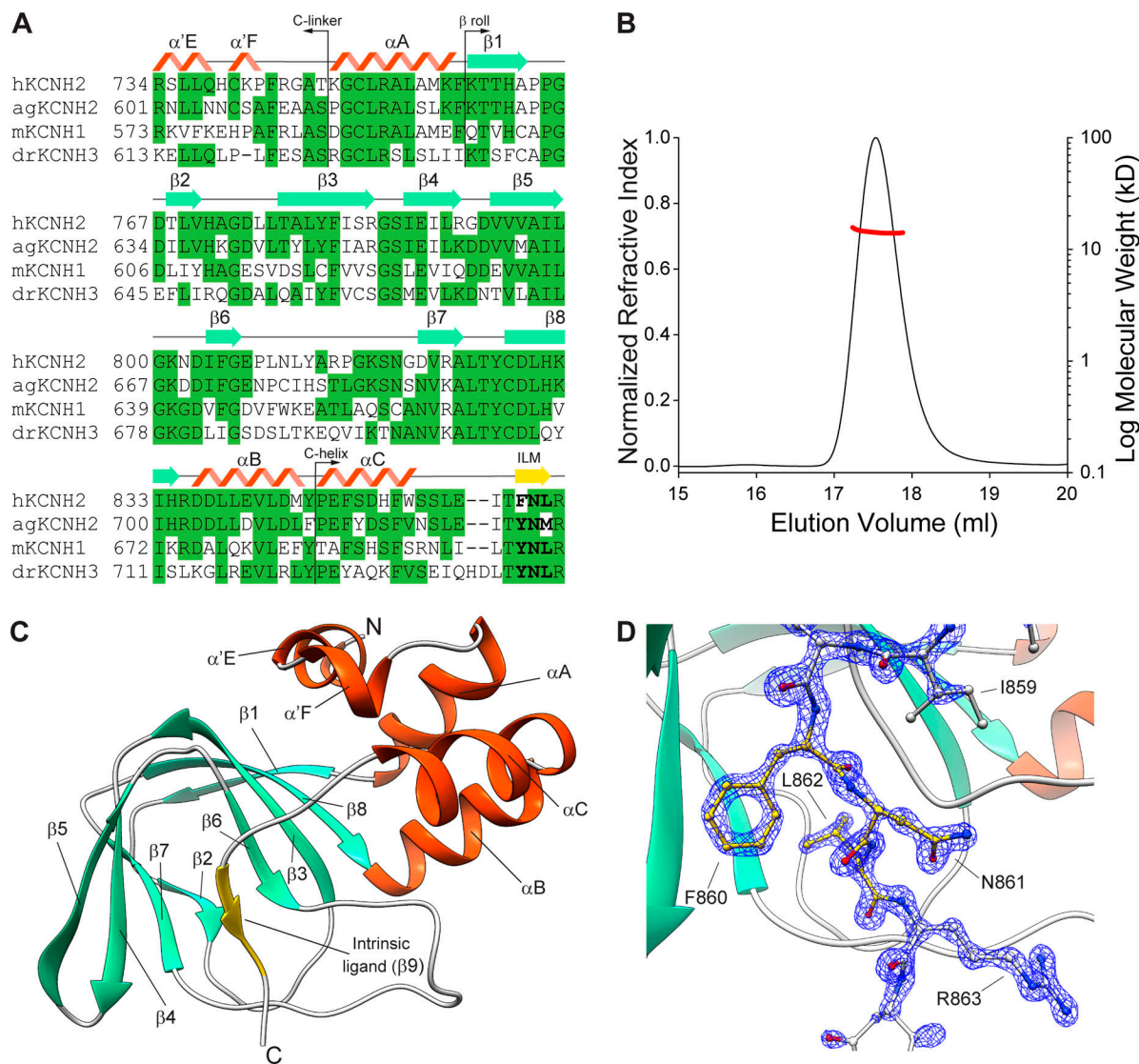
Ben-Bassat et al.
A vital salt-bridge in KCNH2 CNBHD

Journal of General Physiology 4 of 12
https://doi.org/10.1085/jgp.201912505

Figure 1. Structure of hKCNH2 CNBHD. (A) Sequence alignment of the CNBHD from various KCNH family members whose structures are available. Secondary structure of hKCNH2 is indicated above the sequence. α helices and β-strands are in orange and green, respectively, except for the intrinsic ligand motif (ILM), which is yellow. Loops and nonhelical secondary structures are marked as solid gray lines. Residues conserved in KCNH channels are shown in green. The intrinsic ligand motif is bolded. **(B)** SEC-MALS analysis of the purified hKCNH2 CNBHD. The black curve represents the normalized refractive index, and the red curve indicates the calculated molecular weight in kilodaltons. **(C)** Structure of hKCNH2 CNBHD in cartoon representation, colored according to its secondary structure as in A. **(D)** A detailed illustration of the intrinsic ligand (yellow) and flanking residues (gray) shown as sticks and colored by element, overlaid with 2Fo-Fc map contoured at 3σ (blue mesh).

The hKCNH2 CNBHD x-ray and solution NMR structures differ

Recently, the solution structure of the CNBHD of hKCNH2 was determined using NMR (Li et al., 2016). Interestingly, while the superposition of most of the CNBHD (K759-D865) of the calculated ensemble demonstrated a backbone atoms root mean square deviation of 0.49 Å, suggesting a tight and rigid fold in solution, the initial part of the C-linker (R734-P742) displayed high conformational variability (Fig. 2 A). Thus, in order to discern whether some of the hKCNH2 CNBHD solution conformations, sampled by the NMR, are shared with its crystal structure, resolved from a tightly packed environment, we next compared the two structures (Fig. 2 B). This comparison revealed several conformational differences. Specifically, while the crystal structure (Fig. 2 B, green) clearly indicates

that the remnant C-linker maintains it secondary structure and consists of helices α′E and α′F, the solution structure (Fig. 2 B, blue) reveals an almost complete unfolding of this region, with a structural pivot observed at G749. Of note, as the C-linker of the NMR sample is preceded by an N-terminal hexa-histidine purification tag and a TEV protease recognition site, due to the reported decreased solubility following proteolysis, the observed flexibility of this region in solution may stem from this nonnative sequence addition. Moreover, helices αB and αC show a rigid-body displacement of 8.1 Å (S851-S851; cβ-cβ), resulting from a spatial vacancy due to the complete loss of secondary structure of the α′F helix, associated with the destabilization of the C-linker. Importantly, while the αC-β9 linker is affected by these rearrangements,
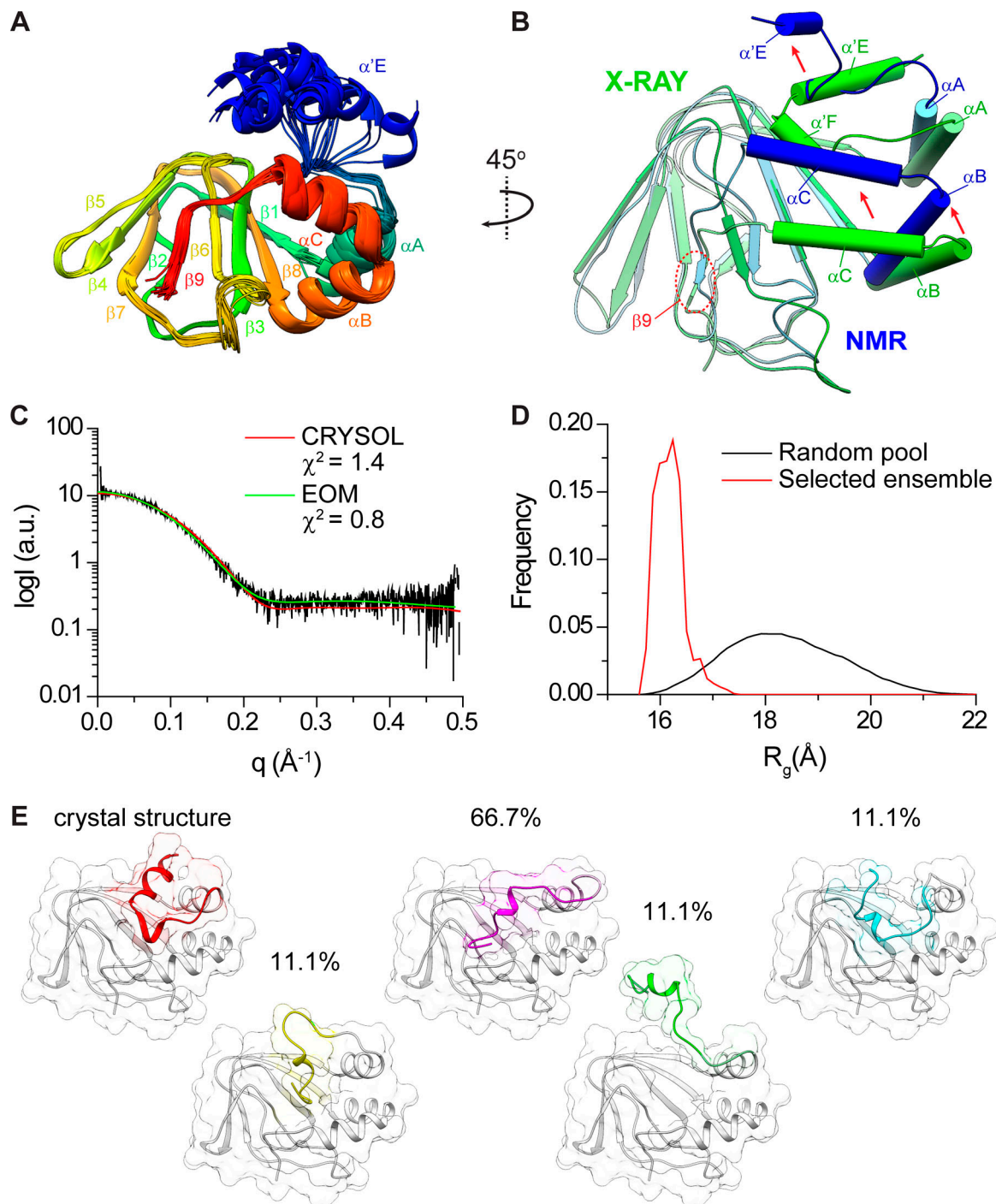
Figure 2. **Solution structure of hKCNH2 CNBHD. (A)** Rainbow-colored depiction of the solution NMR structure ensemble (Protein Data Bank accession no. 2N7G) overlay. **(B)** Superposition of the crystal (green) and NMR (ensemble 1; blue) structures of hKCNH2 CNBHD. The β-roll was used as the alignment anchor. The rigid-body displacement between the overlaid structures is indicated by red arrows. The intrinsic ligand is highlighted by a red circle. **(C)** The experimental SAXS curve of hKCNH2 CNBHD (black curve) was fit using CRYSOL or EOM, as indicated. **(D)** Random R_g pool (black curve) and EOM-selected ensemble distribution of the CNBHD (red curve). **(E)** Representative conformations of hKCNH2 CNBHD selected in the EOM analyses. The relative frequency of each conformation in the selected ensemble is indicated. The remnant C-linker domains, acting as the flexible region, are presented in various colors.

the intrinsic ligand itself maintains its spatial localization (Fig. 2 B).

To determine whether the structural variability observed stems from differences in the experimental environments, we proceeded with SAXS analysis of the hKCNH2 construct used for

crystallization, subjected to an identical purification scheme. Following data collection, we used CRYSOL (Svergun et al., 1995) to calculate the solution scattering originating from the crystal structure in order to compare it with the experimental SAXS curve. The crystallographic structure demonstrated a reasonable

match with the observed solution scattering curve, with $\chi^2 = 1.4$ (Fig. 2 C and Table 2). Next, to explore the possible flexibility of the N-terminus, as observed in the solution NMR structure (Fig. 2 A), we employed the EOM analysis (Bernadó et al., 2007). This approach utilizes an averaged theoretical scattering intensity, derived from an ensemble of conformations, for experimental SAXS data fitting, thus enabling the determination of conformational distributions in solution. First, a random pool of 10,000 conformations was obtained by constructing the residues P742–T747, based on stereochemical restraints. Next, the ensemble of conformations that best fit the data were chosen using a genetic algorithm. Importantly, the selected ensemble fits the data very well ($\chi^2 = 0.8$; Fig. 2 C and Table 2), displaying a narrow distribution of tightly packed conformations (Fig. 2 D). Selected conformers from the random pool, displaying the greatest abundance in the selected ensemble, are presented in Fig. 2 E.

Next, in order to determine whether the NMR data obtained in solution could also be used to fit the SAXS data, we employed the EOM analysis on this ensemble (Fig. S1). Given the compact and rigid CNBHD structure and the multiple conformations observed using NMR for the remnant C-linker domain, this analysis resulted in a good fit ($\chi^2 = 0.84$). However, of the 20 reported NMR states, only two were required to fit the data. Thus, the low-resolution SAXS data could not discern between the different conformations of the αB and αC helices, demonstrating a rigid-body displacement in the NMR ensemble relative to the crystallographic structure (Fig. 2 B). However, the conformation resolved in the crystal structure fits the EM map of the full-length KCNH2 channel (Fig. S2). Together, the hKCNH2 CNBHD demonstrates an overall high rigidity in solution, occupying a narrow conformational distribution.

The intrinsic ligand of hKCNH2

First identified in the structure of the CNBHD from *Danio rerio* (zebrafish) KCNH3 (zKCNH3; zELK; Brelidze et al., 2012), all members of the KCNH family share a unique intrinsic ligand within their canonical CNBHDs (Fig. 1 A). In hKCNH2, this short β-strand (β9) consists of the [860]FNL[862] tripeptide, forming direct interactions with the cavity of the β-roll (Fig. 1 D). While the intrinsic ligand is rather conserved, several mild sequence differences exist within the KCNH family. Specifically, the first position of the intrinsic ligand in zKCNH3 (Brelidze et al., 2012), *Anopheles gambiae* (mosquito) KCNH2 (agKCNH2; agERG; Brelidze et al., 2013), and mKCNH1 (Marques-Carvalho et al., 2012) is a tyrosine residue, positioned in an analogous location as the purine ring of cAMP, when bound to HCN2 channels (Zagotta et al., 2003). Furthermore, this tyrosine participates in hydrogen bond formation with either N697 (drKCNH3) or K658 (agKCNH2; Fig. 1 A), suggesting a possible role for its hydroxyl moiety in the spatial organization of the intrinsic ligand within the β-roll. Conversely, in hKCNH2 this tyrosine is replaced with F860, while the overall fold of the CNBHD is overwhelmingly conserved (Fig. 1 D). Thus, a different interaction mechanism must underlie the spatial organization of the intrinsic ligand in hKCNH2. Our structure demonstrates that the position of F860 is governed by a hydrophobic interaction with I789 (5.3 Å; cβ-cβ)

and a cation-π interaction with R791 (3.4 Å; $R791_{NH1}$-$F860_{C\zeta}$), both localized to the β4 strand, and a hydrophobic interaction with L862 of the intrinsic ligand itself (Fig. 3 A). Indeed, the cavity of the CNBHD is devoid of water molecules, supporting the hydrophobic nature of this interaction network. Furthermore, we detected an additional supportive polar interaction network (Fig. 3 A), likely playing a crucial role in supporting the intrinsic ligand conformation and normal channel function (see below). Thus, while structurally conserved, the molecular determinants underlying the spatial positioning of the intrinsic ligand differ among KCNH family members.

An intrinsic ligand-stabilizing salt-bridge is crucial for hKCNH2 channel function

Our structure of the CNBHD of hKCNH2 reveals that the intrinsic ligand is anchored to the β-roll through an intricate network of polar and charged interactions. Indeed, close examination of this region shows that the β9 strand is juxtaposed in parallel with a β-sheet consisting of roughly one half of the canonical β-roll (β6-β3-β8; Fig. 1 C). This spatial organization is supported by several protein backbone (I804-F860, G806-L862, and N819-L862) and side chain–backbone (T859-I804, R863-N861, N819-N861, and N819-R863) hydrogen bonds (Fig. 3 A). Importantly, additional to these bonds, we detected a single, strategically localized salt-bridge formed between E807 and R863 (Fig. 3 B). Indeed, the spatial organization of this salt-bridge suggests it participates in stabilization of the intrinsic ligand fold. However, this salt-bridge was not observed either in the NMR structure of the isolated CNBHD (Fig. 3 C) or in the cryo-EM structure of the intact channel (Fig. 3 D).

Previously, charge reversal of E807 (E807K) was shown to result in a complete loss of channel function (Cui et al., 2001), indicating the functional importance of the newly identified salt-bridge. In accordance, prediction of the E807K effect on the stability of the CNBHD, using the mutation cutoff scanning matrix (mCSM) approach (Pires et al., 2014), deemed this mutation destabilizing ($\Delta\Delta G = -0.766$ kcal/mol). Thus, to further explore the contribution of an intact salt-bridge for normal channel function, we introduced charge-reversal mutations to both positions and tested the properties in *Xenopus* oocytes using a two-electrode voltage clamp. Similar to the previously reported results, E807K abolished channel function and no currents could be detected (Fig. 4 A). Moreover, E807R, recapitulating a full charge reversal between the salt-bridge positions, also failed to demonstrate detectable currents (Fig. 4 A), consistent with the mCSM prediction ($\Delta\Delta G = -0.622$ kcal/mol). Next, we also examined the effect of introducing a charge-reversal mutation, R863E, to the salt-bridge counterpart position. Unexpectedly, the mCSM server predicted a negligible effect of this mutation on protein stability ($\Delta\Delta G = 0.024$ kcal/mol). Indeed, the R863E mutant produced currents reminiscent of the WT channel (Fig. 4 A; $V_{50} = -27.13 \pm 0.55$, $n = 15$). This observation could result from alternative interaction modes of R863E or E807, or both, in the mutated channel. However, despite the lack of a significant effect of the R863E mutation, its introduction in the context of either E807K or E807R resulted in current rescue (Fig. 4 A). Analysis of the peak amplitudes of the tail currents, measured in response to
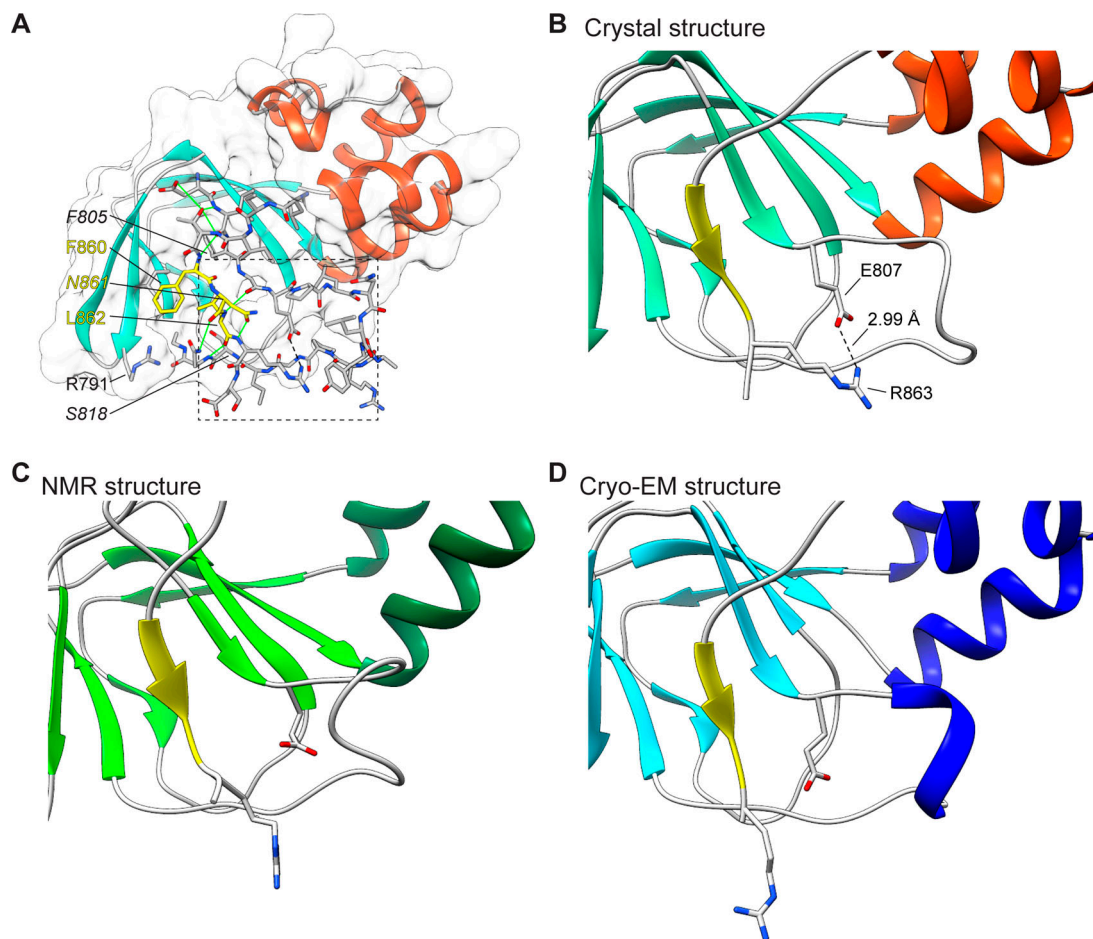
Ben-Bassat et al.
A vital salt-bridge in KCNH2 CNBHD

Journal of General Physiology
https://doi.org/10.1085/jgp.201912505

7 of 12

Figure 3. **The intrinsic ligand interaction network. (A)** Cartoon and surface representation of the CNBHD scaffolding region. Residues that interact with or stabilize the intrinsic ligand are shown as sticks. Intrinsic ligand residues are colored and labeled in yellow, and LQTS-related residues are highlighted in italic. The cation-π interaction R791 is indicated. Atoms interacting via hydrogen bonds and salt-bridge are connected with green and dashed black lines, respectively. **(B–D)** Blowout of the hKCNH2 E807-R863 salt-bridge (B) and the identical region of the NMR (Protein Data Bank accession no. 2N7G; C) and cryo-EM (Protein Data Bank accession no. 5VA1; D) structures. The region shown corresponds to the box indicated in A. The intrinsic ligand motif is indicated by a yellow arrow throughout.

a series of step pulses between –80 and 40 mV in 10-mV increments, followed by a subsequent step pulse to –40 mV, demonstrated comparable current amplitudes (Fig. 4 A). The G–V relationships further demonstrated WT-like voltage dependency (WT V_{50} = –28.38 ± 0.51 mV, n = 23; E807K-R863E V_{50} = –30.71 ± 0.30, n = 25; E807R-R863E V_{50} = –32.38 ± 0.36, n = 7; Fig. 4 C). Thus, the ability of R863E to rescue the phenotype of both E807K and E807R supports the existence and functional significance of the salt-bridge.

Next, we investigated the deactivation kinetics of the charge-reversal mutants. Deactivating current traces of WT and mutants were obtained by a step activation to 20 mV, followed by deactivation pulses ranging from –40 to –80 mV (Fig. 4 B). To determine the slow and fast time constants, tail currents were fit with a double exponential function (τ_{slow} and τ_{fast}, respectively). Intriguingly, although showing an overall similar voltage dependency (Fig. 4 C), the E807K/R863E double mutants combination displayed significantly accelerated deactivation kinetics compared with the characteristic slow deactivation of the WT channel (Fig. 4 D). Specifically, while the WT channel deactivation

followed a relatively slow time course (τ_{slow} = 674 ± 30 ms and τ_{fast} = 101 ± 4 ms at –60 mV, n = 10), the E807K/R863E combination demonstrated faster kinetics (τ_{slow} = 397 ± 15 ms and τ_{fast} = 80 ± 2 ms at –60 mV, n = 17; P < 0.001 for both time constants). Moreover, analysis of the fractional contribution of the fast and slow components showed that while the WT channels demonstrated a voltage-insensitive balance, leaning toward the slow component, the fast component dominated the double mutant kinetics at more hyperpolarized potentials (n = 17; P < 0.001; Fig. 4 D).

The salt-bridge charge-reversal mutation pair E807K/R863E resulted in faster channel deactivation kinetics (Fig. 4 D) while keeping voltage dependency unaffected (Fig. 4 C). A possible gating mechanism accommodating for these two effects may involve activation kinetics acceleration. Indeed, perturbation of the only inter-domain salt-bridge observed before in the previously reported structure of the mKCNH1 eag domain–CNBHD complex (R57-D642; Fig. 5 A) resulted in acceleration of channel activation (Haitin et al., 2013). Thus, to discern whether a similar mechanism is present here, we analyzed the activation
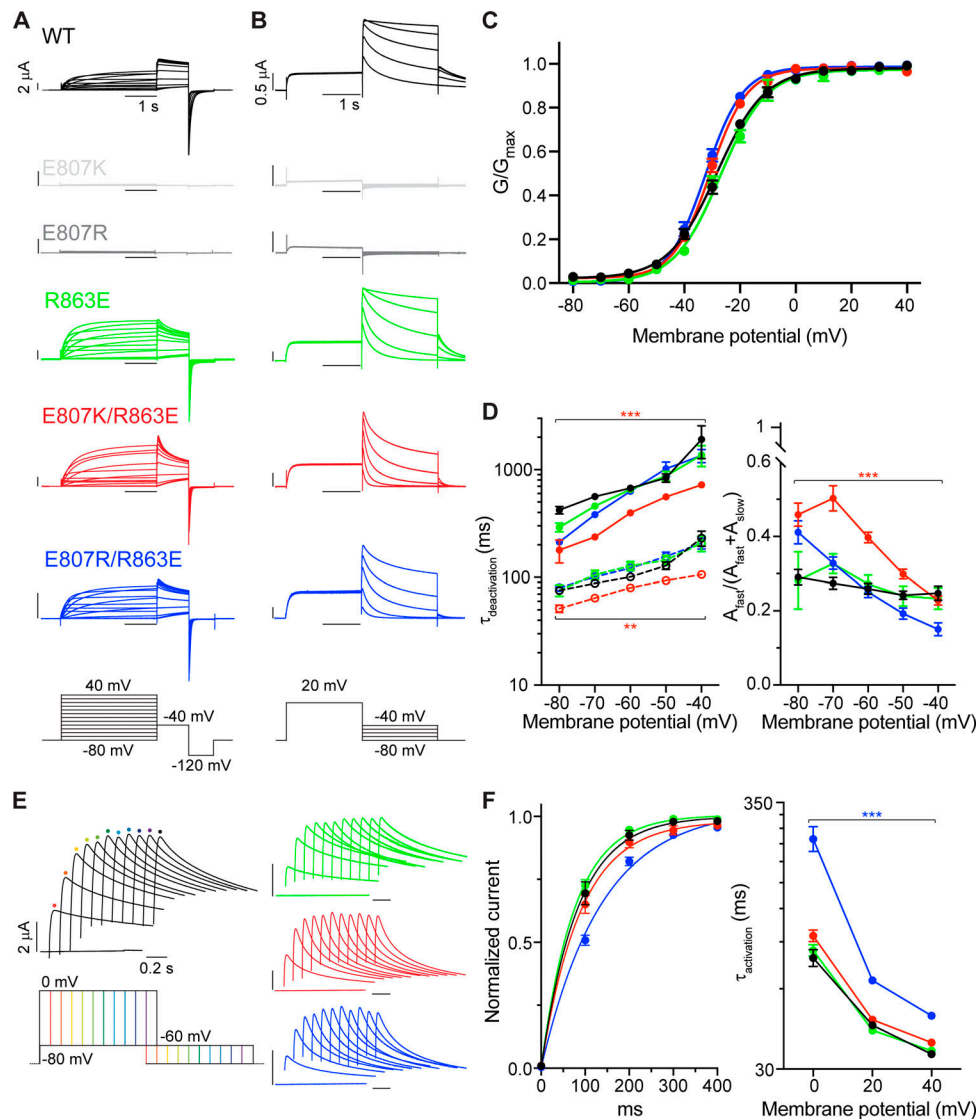
Figure 4. **Functional analysis of the E807-R863 salt-bridge. (A)** Representative current recordings from WT (black), E807K (light gray), E807R (gray), E807K/R863E (red), E807R/R863E (blue), and R863E (green). The step pulse protocol is depicted at the bottom. **(B)** Representative tail current recordings for measurement of channel deactivation kinetics. The step pulse protocol is depicted at the bottom. **(C)** G–V relationships. The peak amplitudes of the tail currents at −40 mV were normalized to the maximum tail current in each cell, and the average values were plotted as a function of the membrane potential. The V_{50} values were obtained by fitting the G–V relationships to a Boltzmann function (error bars indicate SEM; n = 7–25 cells). **(D)** τ_{slow} and τ_{fast} values of deactivation represented as solid and dashed lines, respectively (left). Each deactivating tail current was fit to a double exponential function to calculate the slow and fast time constants, and the average values were plotted as a function of membrane potential. Fractional fast component contribution, $A_{fast}/(A_{fast} + A_{slow})$, is presented as a function of membrane potential (right; error bars indicate SEM; n = 7–17 cells; **, P < 0.01; ***, P < 0.001, repeated-measures two-way ANOVA). **(E)** Representative activation current recordings (0 mV) from WT and conductive mutants, color coded as in A. Cells were held at −80 mV, followed by a depolarizing voltage step (to 0, 20, and 40 mV) for increasing durations. The depolarizing test pulses were followed by a fixed duration step pulse to −60 mV. Finally, the voltage was stepped back to −80 mV. The color-coded voltage protocol shown at the bottom matches the colored circles above the WT representative traces. **(F)** The activation kinetics were evaluated by the mono-exponential fit of the increase in the peak tail current amplitude in response to an incremental increase in test pulse duration (left). Activation curves of WT and conductive mutants (left) $\tau_{activation}$ values at 0, 20, and 40 mV (right) are presented (error bars indicate SEM; n = 7–17 cells; ***, P < 0.001, repeated-measures two-way ANOVA).

kinetics of the WT and mutants by measuring the tail current amplitude dependence on the increase of the preceding test potential duration (Fig. 4 E). Next, a mono-exponential function was employed to fit the activation time course and obtain the $\tau_{activation}$ time constant. Intriguingly, while the activation kinetics of E807K/R863E was not significantly changed throughout the voltage clamp regimens tested, the E807R/R863E mutant

surprisingly demonstrated slower activation (n = 6–9; P < 0.001; Fig. 4 F) despite sharing similar deactivation kinetics with the WT channel (Fig. 4 D). Thus, the activation and deactivation kinetics of the double charge-reversal mutants are affected by the identity of the residue at position 807. Together, the crystal structure of hKCNH2 CNBHD reveals a novel functionally important E807-R863 salt-bridge.
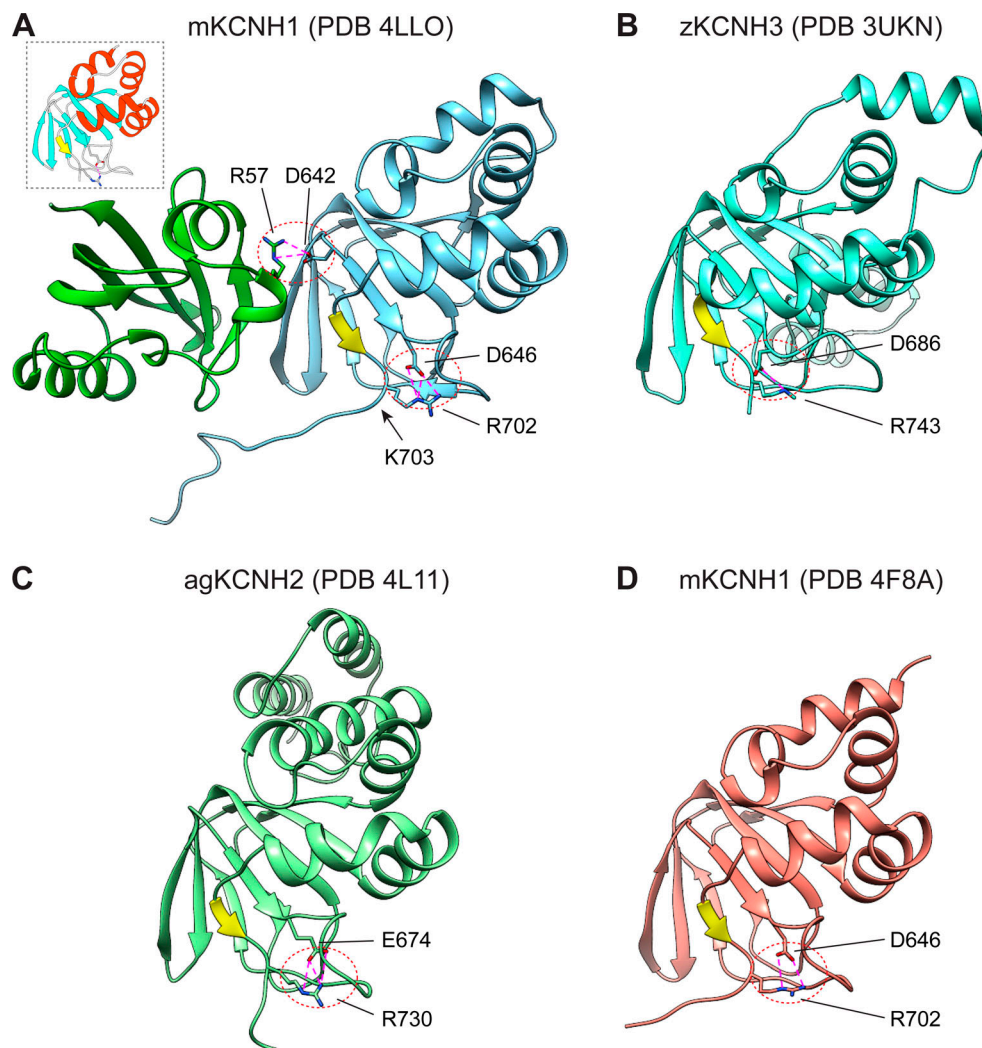
Figure 5. Structural comparisons with select KCNH CNBHD crystal structures. (A) Structure of the eag domain–CNBHD complex from mKCNH1. The N-terminal eag domain is green, and the C-terminal CNBHD is blue. Inter-domain (R57-D642) and CNBHD (D646-R702) salt-bridges are indicated in magenta. The black arrow indicates the post-CNBHD kink. The CNBHD of hKCNH2 is presented for orientation (inset). **(B–D)** Salt-bridges of the CNBHDs of zKCNH3 (D686-R743; B), agKCNH2 (E674-R730; C), and mKCNH1 (D) are indicated as in A. Intrinsic ligands are indicated by a yellow arrow throughout.

Discussion

In this study, we used various biophysical approaches to resolve the molecular determinants involved in the structural organization of hKCNH2 CNBHD. Following the initial characterization of the purified CNBHD using SEC-MALS (Fig. 1 B), we crystallized and obtained the structure of this domain at high resolution. This structure, solved at an unprecedented resolution for a CNBHD of 1.5 Å (Brelidze et al., 2012, 2013; Marques-Carvalho et al., 2012; Haitin et al., 2013), provided exquisite molecular details into the spatial organization of the intrinsic ligand (Fig. 1 D). Importantly, the crystallographic structure is in high agreement with the solution scattering profile (Fig. 2, C–E) and the recent NMR analysis of hKCNH2 (Li et al., 2016). Importantly, the atomic structure resolution identified a novel salt-bridge that was not previously resolved (Fig. 3). Strikingly, electrophysiological analysis of charge-reversal mutations revealed its crucial role for hKCNH2 function (Fig. 4).

KCNH channels are widely expressed in the human body and play central roles in numerous physiological and pathophysiological processes. hKCNH2 channels, arguably the prominent pathophysiologically relevant family members, have a critical role in human cardiac repolarization. Unlike the cyclic nucleotide–gated and HCN channels, the CNBHD of KCNH encompasses the intrinsic ligand, spatially replacing the cyclic nucleotides, blocking their binding site (Brelidze et al., 2012; Marques-Carvalho et al., 2012; Haitin et al., 2013). Ever since its identification (Brelidze et al., 2012; Marques-Carvalho et al., 2012), the intrinsic ligand has been shown to play a crucial role in KCNH channel family function (Brelidze et al., 2013; Zhao et al., 2017; Codding and Trudeau, 2019). Nevertheless, the mechanism by which it participates in channel gating modulation remains ambiguous. Indeed, possible modulatory mechanisms may involve the interaction of the CNBHD with the canonical N-terminal eag domain (Gianulis et al., 2013; Haitin et al., 2013), together with alterations of

Ben-Bassat et al.
A vital salt-bridge in KCNH2 CNBHD

Journal of General Physiology   10 of 12
https://doi.org/10.1085/jgp.201912505

the conformational space occupied by the CNBHD and its associated C-linker (Zhao et al., 2017).

Over the past years, major strides forward have been made toward a comprehensive elucidation of the structure–function relations governing KCNH channel gating, culminating in the determination of the structure of an intact hKCNH2 channel by cryo-EM (Wang and MacKinnon, 2017). This groundbreaking milestone provided the long-sought molecular characterization of hKCNH2 transmembrane domain, depicting the voltage sensors in an active conformation, explaining their notorious sensitivity to drug-induced blockade and shedding light on the fast inactivation mechanism. However, due to the inherent limitation of cryo-EM in providing high-resolution data of domains displaying spatial heterogeneity, as observed for the intracellular eag domain and CNBHD of hKCNH2, structural information regarding these regions is largely limited to their overall secondary structure fold and relative orientation. Therefore, combining the advantages of high-resolution x-ray crystallography with those of cryo-EM offers the opportunity to resolve the exact interaction network underlying the occupancy of the CNBHD by the intrinsic ligand and to interpret this information in the context of an intact hKCNH2 channel. Moreover, this powerful combination highlights the everlasting relevance of crystallographic data in modern and future structural investigations.

Previous studies focused on the intrinsic ligand itself and its effect on the interaction between the CNBHD and the eag domain (Zhao et al., 2017; Codding and Trudeau, 2019). Here, based on our structural analysis, we focused on a putative salt-bridge that was deemed important for stabilization of the intrinsic ligand. Comparison of our structure with previously determined crystal structures of KCNH CNBHD homologues revealed that the spatial organization leading to the formation of the E807-R863 salt-bridge is highly conserved (Fig. 5). Indeed, CNBHD structures from zKCNH3 (Fig. 5 B), agKCNH2 (Fig. 5 C), and mKCNH1 (Fig. 5 D) show that positions homologous to E807 and R863 of hKCNH2 are nearly identically situated. As shown here, consistent with the high level of structural conservation, the salt-bridge plays a role in channel function (Fig. 4). Previously, based on electrophysiological and spectroscopic studies of intact channels, it was suggested that the interaction between the CNBHD and the eag domain plays a role in the functional regulation of KCNH channels (Dai and Zagotta, 2017; Codding and Trudeau, 2019). However, the only available high-resolution structure of the intracellular complex of KCNH channels remains the cocrystal structure of the mKCNH1 eag domain–CNBHD (Haitin et al., 2013). Interestingly, structural alignment with the CNBHD of the KCNH1 intracellular complex revealed a kink immediately following the conserved salt-bridge (K703), with the post-CNBHD region, encompassing a calmodulin binding site, cradling the eag domain (Fig. 5 A). Thus, it appears that the salt-bridge serves as a linchpin, limiting the conformational landscape of the intrinsic ligand while allowing interaction of the post-CNBHD region with the eag domain in mKCNH1 channels. This can support recent results demonstrating that the intrinsic ligand undergoes a defined conformational change during voltage-dependent channel potentiation, rather than dissociation from its binding pocket upon relative rearrangement between the eag domain and the CNHBD (Dai et al., 2018).

In conclusion, this study provides molecular insights into the structural organization of the hKCNH2 CNBHD in an unprecedented resolution. This structure revealed a previously overlooked salt-bridge playing a role in channel function. Structural comparison with the intracellular complex of mKCNH1, together with electrophysiological studies, suggests that this salt-bridge is strategically positioned to support both the organization of the intrinsic ligand and the intracellular complex interface. As most KCNH channels differ in their post-CNBHD region, future studies are needed to address the functional role of this salt-bridge during channel gating and regulation in different family members.

References

Adams, P.D., P.V. Afonine, G. Bunkóczi, V.B. Chen, I.W. Davis, N. Echols, J.J. Headd, L.W. Hung, G.J. Kapral, R.W. Grosse-Kunstleve, et al. 2010. PHENIX: a comprehensive Python-based system for macromolecular structure solution. *Acta Crystallogr. D Biol. Crystallogr.* 66:213–221. https://doi.org/10.1107/S0907444909052925

Anderson, C.L., B.P. Delisle, B.D. Anson, J.A. Kilby, M.L. Will, D.J. Tester, Q. Gong, Z. Zhou, M.J. Ackerman, and C.T. January. 2006. Most LQT2 mutations reduce Kv11.1 (hERG) current by a class 2 (trafficking-deficient) mechanism. *Circulation.* 113:365–373. https://doi.org/10.1161/CIRCULATIONAHA.105.570200

Bernadó, P., E. Mylonas, M.V. Petoukhov, M. Blackledge, and D.I. Svergun. 2007. Structural characterization of flexible proteins using small-angle X-ray scattering. *J. Am. Chem. Soc.* 129:5656–5664. https://doi.org/10.1021/ja069124n

Bianchi, L., B. Wible, A. Arcangeli, M. Taglialatela, F. Morra, P. Castaldo, O. Crociani, B. Rosati, L. Faravelli, M. Olivotto, and E. Wanke. 1998. herg

encodes a K+ current highly conserved in tumors of different histogenesis: a selective advantage for cancer cells? *Cancer Res.* 58:815–822.

Brelidze, T.I., A.E. Carlson, and W.N. Zagotta. 2009. Absence of direct cyclic nucleotide modulation of mEAG1 and hERG1 channels revealed with fluorescence and electrophysiological methods. *J. Biol. Chem.* 284:27989–27997. https://doi.org/10.1074/jbc.M109.016337

Brelidze, T.I., A.E. Carlson, B. Sankaran, and W.N. Zagotta. 2012. Structure of the carboxy-terminal region of a KCNH channel. *Nature.* 481:530–533. https://doi.org/10.1038/nature10735

Brelidze, T.I., E.C. Gianulis, F. DiMaio, M.C. Trudeau, and W.N. Zagotta. 2013. Structure of the C-terminal region of an ERG channel and functional implications. *Proc. Natl. Acad. Sci. USA.* 110:11648–11653. https://doi.org/10.1073/pnas.1306887110

Chen, J., A. Zou, I. Splawski, M.T. Keating, and M.C. Sanguinetti. 1999. Long QT syndrome-associated mutations in the Per-Arnt-Sim (PAS) domain of HERG potassium channels accelerate channel deactivation. *J. Biol. Chem.* 274:10113–10118. https://doi.org/10.1074/jbc.274.15.10113

Codding, S.J., and M.C. Trudeau. 2019. The hERG potassium channel intrinsic ligand regulates N- and C-terminal interactions and channel closure. *J. Gen. Physiol.* 151:478–488. https://doi.org/10.1085/jgp.201812129

Collaborative Computational Project Number 4. 1994. The CCP4 suite: programs for protein crystallography. *Acta Crystallogr. D Biol. Crystallogr.* 50:760–763. https://doi.org/10.1107/S0907444994003112

Craven, K.B., and W.N. Zagotta. 2006. CNG and HCN channels: two peas, one pod. *Annu. Rev. Physiol.* 68:375–401. https://doi.org/10.1146/annurev.physiol.68.040104.134728

Cui, J., A. Kagan, D. Qin, J. Mathew, Y.F. Melman, and T.V. McDonald. 2001. Analysis of the cyclic nucleotide binding domain of the HERG potassium channel and interactions with KCNE2. *J. Biol. Chem.* 276:17244–17251. https://doi.org/10.1074/jbc.M010904200

Curran, M.E., I. Splawski, K.W. Timothy, G.M. Vincent, E.D. Green, and M.T. Keating. 1995. A molecular basis for cardiac arrhythmia: HERG mutations cause long QT syndrome. *Cell.* 80:795–803. https://doi.org/10.1016/0092-8674(95)90358-5

Dai, G., and W.N. Zagotta. 2017. Molecular mechanism of voltage-dependent potentiation of KCNH potassium channels. *eLife.* 6:e26355. https://doi.org/10.7554/eLife.26355

Dai, G., Z.M. James, and W.N. Zagotta. 2018. Dynamic rearrangement of the intrinsic ligand regulates KCNH potassium channels. *J. Gen. Physiol.* 150:625–635. https://doi.org/10.1085/jgp.201711989

Emsley, P., and K. Cowtan. 2004. Coot: model-building tools for molecular graphics. *Acta Crystallogr. D Biol. Crystallogr.* 60:2126–2132. https://doi.org/10.1107/S0907444904019158

Ganetzky, B., G.A. Robertson, G.F. Wilson, M.C. Trudeau, and S.A. Titus. 1999. The eag family of K+ channels in Drosophila and mammals. *Ann. N. Y. Acad. Sci.* 868(1 MOLECULAR AND):356–369. https://doi.org/10.1111/j.1749-6632.1999.tb11297.x

Gianulis, E.C., Q. Liu, and M.C. Trudeau. 2013. Direct interaction of eag domains and cyclic nucleotide-binding homology domains regulate deactivation gating in hERG channels. *J. Gen. Physiol.* 142:351–366. https://doi.org/10.1085/jgp.201310995

Gustina, A.S., and M.C. Trudeau. 2009. A recombinant N-terminal domain fully restores deactivation gating in N-truncated and long QT syndrome mutant hERG potassium channels. *Proc. Natl. Acad. Sci. USA.* 106:13082–13087. https://doi.org/10.1073/pnas.0900180106

Haitin, Y., A.E. Carlson, and W.N. Zagotta. 2013. The structural mechanism of KCNH-channel regulation by the eag domain. *Nature.* 501:444–448. https://doi.org/10.1038/nature12487

Harley, C.A., C.S.H. Jesus, R. Carvalho, R.M.M. Brito, and J.H. Morais-Cabral. 2012. Changes in channel trafficking and protein stability caused by LQT2 mutations in the PAS domain of the HERG channel. *PLoS One.* 7:e32654. https://doi.org/10.1371/journal.pone.0032654

Huffaker, S.J., J. Chen, K.K. Nicodemus, F. Sambataro, F. Yang, V. Mattay, B.K. Lipska, T.M. Hyde, J. Song, D. Rujescu, et al. 2009. A primate-specific, brain isoform of KCNH2 affects cortical physiology, cognition, neuronal repolarization and risk of schizophrenia. *Nat. Med.* 15:509–518. https://doi.org/10.1038/nm.1962

Koch, M.H.J., P. Vachette, and D.I. Svergun. 2003. Small-angle scattering: a view on the properties, structures and structural changes of biological macromolecules in solution. *Q. Rev. Biophys.* 36:147–227. https://doi.org/10.1017/S0033583503003871

Konarev, P.V., V.V. Volkov, A.V. Sokolova, M.H.J. Koch, and D.I. Svergun. 2003. PRIMUS: A Windows PC-based system for small-angle scattering data analysis. *J. Appl. Cryst.* 36:1277–1282. https://doi.org/10.1107/S0021889803012779

Li, Y., H.Q. Ng, Q. Li, and C. Kang. 2016. Structure of the Cyclic Nucleotide-Binding Homology Domain of the hERG Channel and Its Insight into Type 2 Long QT Syndrome. *Sci. Rep.* 6:23712. https://doi.org/10.1038/srep23712

Marques-Carvalho, M.J., N. Sahoo, F.W. Muskett, R.S. Vieira-Pires, G. Gabant, M. Cadene, R. Schönherr, and J.H. Morais-Cabral. 2012. Structural, biochemical, and functional characterization of the cyclic nucleotide binding homology domain from the mouse EAG1 potassium channel. *J. Mol. Biol.* 423:34–46. https://doi.org/10.1016/j.jmb.2012.06.025

McCoy, A.J. 2007. Solving structures of protein complexes by molecular replacement with Phaser. *Acta Crystallogr. D Biol. Crystallogr.* 63:32–41. https://doi.org/10.1107/S0907444906045975

Morais Cabral, J.H., A. Lee, S.L. Cohen, B.T. Chait, M. Li, and R. Mackinnon. 1998. Crystal structure and functional analysis of the HERG potassium channel N terminus: a eukaryotic PAS domain. *Cell.* 95:649–655. https://doi.org/10.1016/S0092-8674(00)81635-9

Morais-Cabral, J.H., and G.A. Robertson. 2015. The enigmatic cytoplasmic regions of KCNH channels. *J. Mol. Biol.* 427:67–76. https://doi.org/10.1016/j.jmb.2014.08.008

Petoukhov, M.V., D. Franke, A.V. Shkumatov, G. Tria, A.G. Kikhney, M. Gajda, C. Gorba, H.D.T. Mertens, P.V. Konarev, and D.I. Svergun. 2012. New developments in the *ATSAS* program package for small-angle scattering data analysis. *J. Appl. Cryst.* 45:342–350. https://doi.org/10.1107/S0021889812007662

Pettersen, E.F., T.D. Goddard, C.C. Huang, G.S. Couch, D.M. Greenblatt, E.C. Meng, and T.E. Ferrin. 2004. UCSF Chimera--a visualization system for exploratory research and analysis. *J Comput Chem.* 25:1605–1612. https://doi.org/10.1002/jcc.20084

Pires, D.E.V., D.B. Ascher, and T.L. Blundell. 2014. mCSM: predicting the effects of mutations in proteins using graph-based signatures. *Bioinformatics.* 30:335–342. https://doi.org/10.1093/bioinformatics/btt691

Puljung, M.C., and W.N. Zagotta. 2013. A secondary structural transition in the C-helix promotes gating of cyclic nucleotide-regulated ion channels. *J. Biol. Chem.* 288:12944–12956. https://doi.org/10.1074/jbc.M113.464123

Rehmann, H., A. Wittinghofer, and J.L. Bos. 2007. Capturing cyclic nucleotides in action: snapshots from crystallographic studies. *Nat. Rev. Mol. Cell Biol.* 8:63–73. https://doi.org/10.1038/nrm2082

Robertson, G.A., J.M. Warmke, and B. Ganetzky. 1996. Potassium currents expressed from Drosophila and mouse eag cDNAs in Xenopus oocytes. *Neuropharmacology.* 35:841–850. https://doi.org/10.1016/0028-3908(96)00113-X

Sanguinetti, M.C., and N.K. Jurkiewicz. 1990. Two components of cardiac delayed rectifier K+ current. Differential sensitivity to block by class III antiarrhythmic agents. *J. Gen. Physiol.* 96:195–215. https://doi.org/10.1085/jgp.96.1.195

Sanguinetti, M.C., and M. Tristani-Firouzi. 2006. hERG potassium channels and cardiac arrhythmia. *Nature.* 440:463–469. https://doi.org/10.1038/nature04710

Sanguinetti, M.C., C. Jiang, M.E. Curran, and M.T. Keating. 1995. A mechanistic link between an inherited and an acquired cardiac arrhythmia: HERG encodes the IKr potassium channel. *Cell.* 81:299–307. https://doi.org/10.1016/0092-8674(95)90340-2

Svergun, D., C. Barberato, and M.H. Koch. 1995. CRYSOL - A program to evaluate X-ray solution scattering of biological macromolecules from atomic coordinates. *J. Appl. Cryst.* 28:768–773. https://doi.org/10.1107/S0021889895007047

Trudeau, M.C., J.W. Warmke, B. Ganetzky, and G.A. Robertson. 1995. HERG, a human inward rectifier in the voltage-gated potassium channel family. *Science.* 269:92–95. https://doi.org/10.1126/science.7604285

Wang, W., and R. MacKinnon. 2017. Cryo-EM structure of the open human ether-à-go-go-related K+ Channel hERG. *Cell.* 169:422–430.e10. https://doi.org/10.1016/j.cell.2017.03.048

Warmke, J., R. Drysdale, and B. Ganetzky. 1991. A distinct potassium channel polypeptide encoded by the Drosophila eag locus. *Science.* 252:1560–1562. https://doi.org/10.1126/science.1840699

Whicher, J.R., and R. MacKinnon. 2016. Structure of the voltage-gated K+ channel Eag1 reveals an alternative voltage sensing mechanism. *Science.* 353:664–669. https://doi.org/10.1126/science.aaf8070

Zagotta, W.N., N.B. Olivier, K.D. Black, E.C. Young, R. Olson, and E. Gouaux. 2003. Structural basis for modulation and agonist specificity of HCN pacemaker channels. *Nature.* 425:200–205. https://doi.org/10.1038/nature01922

Zhao, Y., M.P. Goldschen-Ohm, J.H. Morais-Cabral, B. Chanda, and G.A. Robertson. 2017. The intrinsically liganded cyclic nucleotide-binding homology domain promotes KCNH channel activation. *J. Gen. Physiol.* 149:249–260. https://doi.org/10.1085/jgp.201611701
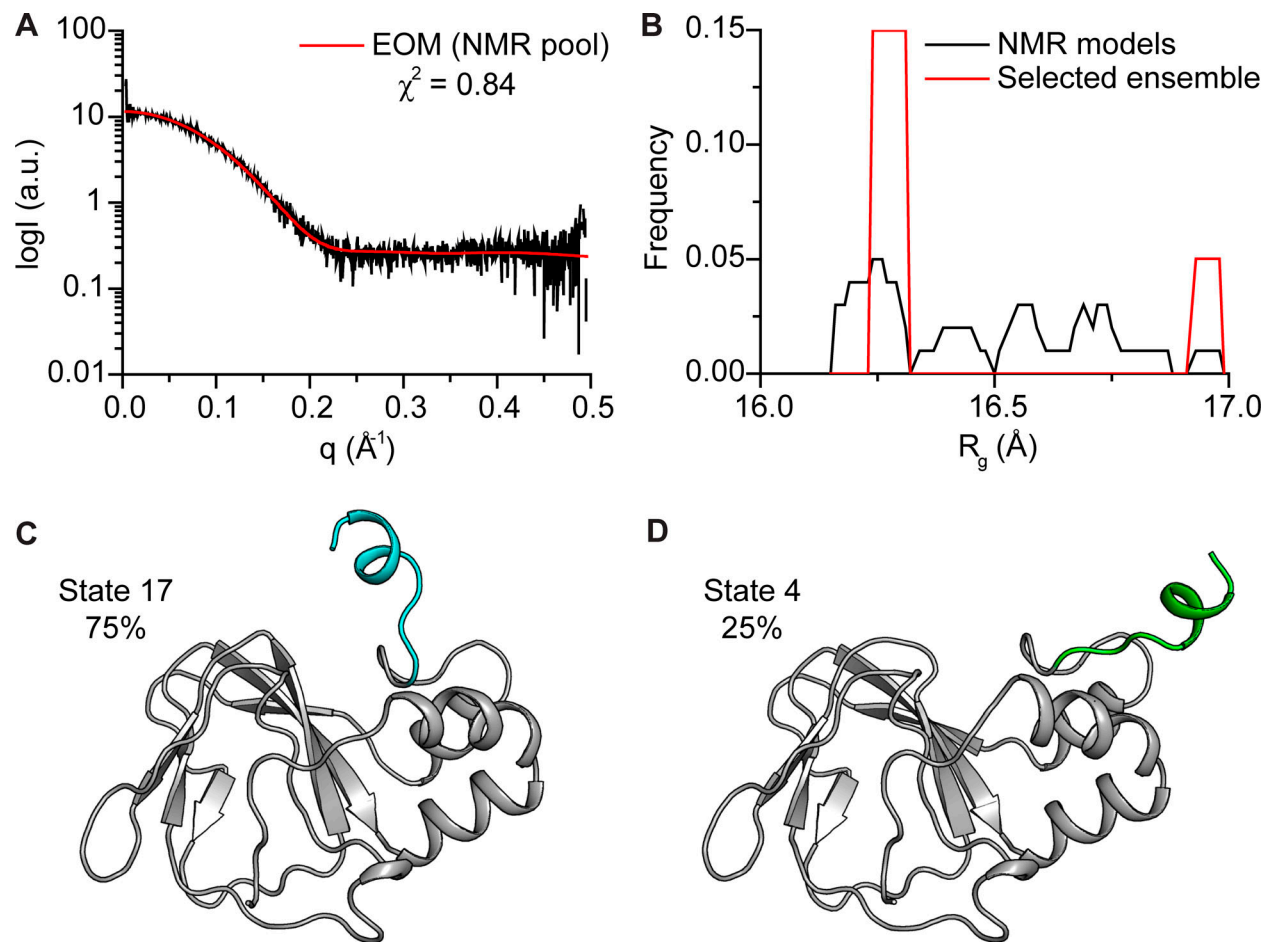
Supplemental material

Figure S1. **hKCNH2 CNBHD EOM analysis using the NMR ensemble. (A)** Experimental SAXS curve of hKCNH2 CNBHD was fit using EOM, with the 20 NMR states serving as an ensemble. **(B)** Random R_g pool consisting of all available NMR conformers (black line) and EOM-selected ensemble distributions of the CNBHD (red line). **(C and D)** Abundance of NMR states (Protein Data Bank accession no. 2N7G) determined by the EOM analysis. The remnant C-linker is highlighted in cyan (C) or green (D).
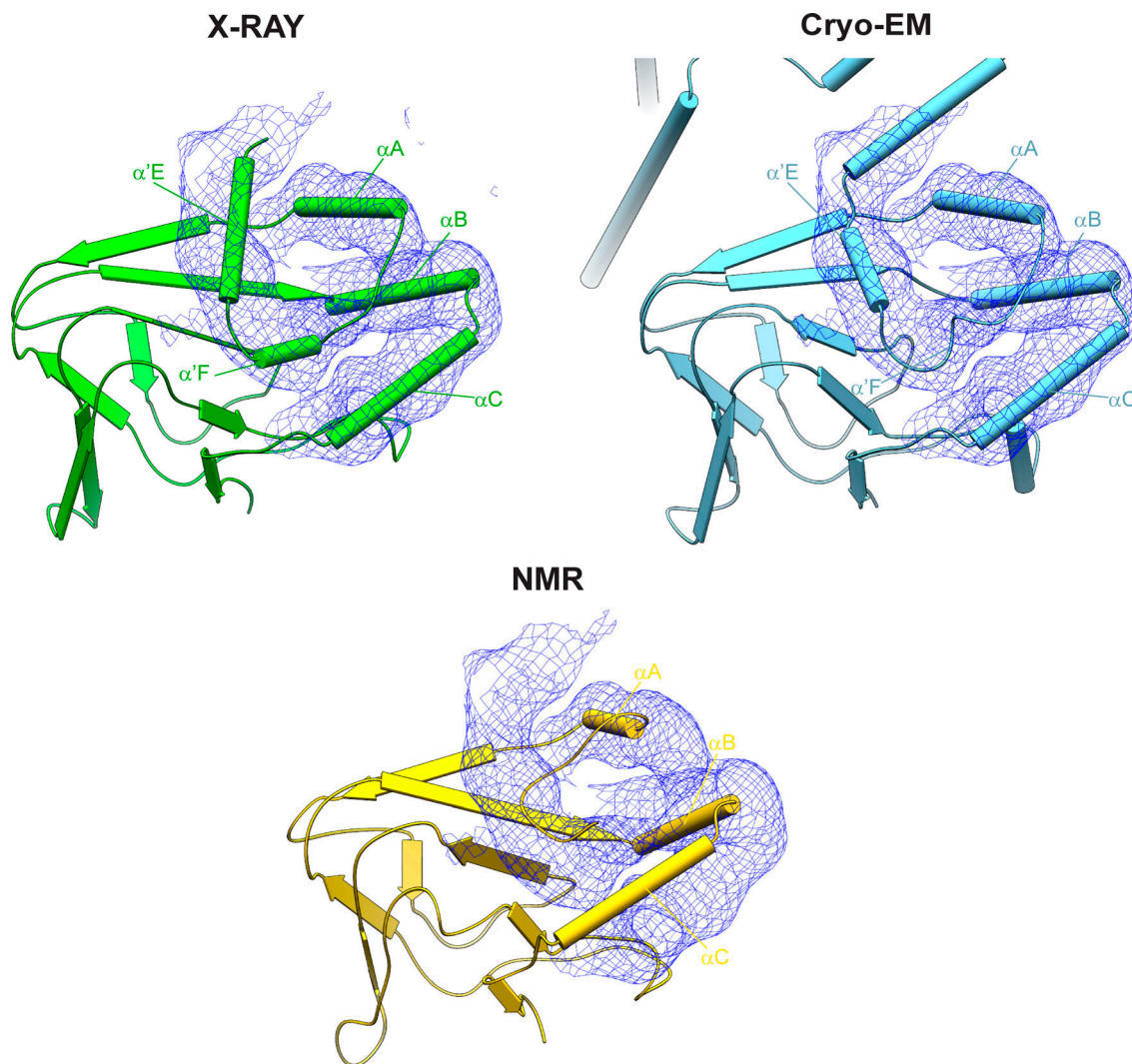
X-RAY

Cryo-EM

NMR

Figure S2.   **Superposition of available hKCNH2 CNBHD structures with the cryo-EM map of the intact channel.** Cartoon representations of the x-ray (green), cryo-EM (cyan), and NMR (yellow) structures of hKCNH2 CNBHD. The cryo-EM map (Protein Data Bank accession no. 5VA1) of the α-helical regions of the CNBHD is shown as blue mesh. The β-barrels of the NMR and x-ray structures were superposed with the cryo-EM model, highlighting the altered conformation of the α helices observed in the NMR structure.